AGU PUBLICATIONS

JGR

Journal of Geophysical Research: Atmospheres

RESEARCH ARTICLE

10.1002/2016JD024875

This article is a companion to *Schäfer et al.* [2016], doi:10.1002/2016JD024876.

Key Points:
- New broadband radiation scheme captures 3-D effects efficiently
- Solves modified two-stream scheme using matrix exponentials
- Validated against 3-D Monte Carlo model in shortwave and longwave

Correspondence to:
R. J. Hogan,
r.j.hogan@ecmwf.int

Citation:
Hogan, R. J., S. A. K.Schäfer, C. Klinger, J. C. Chiu, and B. Mayer (2016), Representing 3-D cloud radiation effects in two-stream schemes: 2. Matrix formulation and broadband evaluation, *J. Geophys. Res. Atmos.*, *121*, doi:10.1002/2016JD024875.

Received 29 JAN 2016
Accepted 29 MAY 2016
Accepted article online 1 JUL 2016

Representing 3-D cloud radiation effects in two-stream schemes: 2. Matrix formulation and broadband evaluation

Robin J. Hogan[1,2], Sophia A. K. Schäfer[2], Carolin Klinger[3], J. Christine Chiu[2], and Bernhard Mayer[3]

[1]European Centre for Medium-Range Weather Forecasts, Reading, UK, [2]Department of Meteorology, University of Reading, Reading, UK, [3]Meteorological Institute, Ludwig Maximilians University, Munich, Germany

Abstract Estimating the impact of radiation transport through cloud sides on the global energy budget is hampered by the lack of a fast radiation scheme suitable for use in global atmospheric models that can represent these effects in both the shortwave and longwave. This two-part paper describes the development of such a scheme, which we refer to as the Speedy Algorithm for Radiative Transfer through Cloud Sides (SPARTACUS). The principle of the method is to add extra terms to the two-stream equations to represent lateral transport between clear and cloudy regions, which vary in proportion to the length of cloud edge as a function of height. The present paper describes a robust and accurate method for solving the coupled system of equations in both the shortwave and longwave in terms of matrix exponentials. This solver has been coupled to a correlated-*k* model for gas absorption. We then confirm the accuracy of SPARTACUS by performing broadband comparisons with fully 3-D radiation calculations by the Monte Carlo model "MYSTIC" for a cumulus cloud field, examining particularly the percentage change in cloud radiative effect (CRE) when 3-D effects are introduced. In the shortwave, SPARTACUS correctly captures this change to CRE, which varies with solar zenith angle between −25% and +120%. In the longwave, SPARTACUS captures well the increase in radiative cooling of the cloud, although it is only able to correctly simulate the 30% increase in surface CRE (around 4 W m^{-2}) if an approximate correction is made for cloud clustering.

1. Introduction

The flow of radiation through cloud sides is currently neglected in the radiation schemes of all general circulation models (GCMs), yet these 3-D effects may have an important effect on the radiation balance. There have been only a few estimates of the global impact of 3-D radiative transfer. *Barker et al.* [2015] used satellite radar and lidar retrievals as input to a broadband Monte Carlo radiation scheme to estimate the effect on shortwave fluxes at the surface and top of atmosphere. They found systematic changes versus solar zenith angle in the sense of 3-D effects making the atmosphere less reflective by around 10 W m^{-2} for overhead Sun and more reflective by around the same amount when the Sun was low in the sky. Since their cloud fields were only two dimensional, they may have underestimated the 3-D effect by as much as 30% [e.g., *Pincus et al.*, 2005]. *Tompkins and Di Giuseppe* [2007] devised a very approximate way to represent shortwave 3-D effects in a 1-D radiation scheme by changing the cloud overlap according to solar zenith angle. When run in a GCM, they reported a globally averaged effect on top-of-atmosphere net fluxes of around 1 W m^{-2}, although they only represented the increased reflection when the Sun is low in the sky, but not the reduced reflection when the Sun is high in the sky. To date there has been no global estimate of the impact of 3-D effects in the longwave at both surface and top of atmosphere, although *Heidinger and Cox* [1996] estimated that for cumulus clouds they can increase the surface cloud radiative effect by around 30%.

Hogan and Shonk [2013] proposed a promising method for introducing 3-D effects into the radiation schemes of GCMs: they added extra terms to the two-stream equations to represent the rate of transport of radiation between clear and cloudy regions in proportion to the length of cloud edge. While demonstrating encouraging agreement with full 3-D calculations in the literature, there were several shortcomings of their study:

1. Their method was applied only to shortwave radiation.
2. The validity of using the exact cloud edge length in the formulation was not tested, and cloud edge length is not a well-defined quantity due to the fractal nature of clouds.

3. Cloud horizontal inhomogeneity was not represented.
4. Their method to solve these equations was overly complicated in the way that radiation passing through cloud sides was "lost" to the system and then reintroduced in separate steps, leading to inaccuracies due to the need to fit exponential functions to the vertical flux distribution many times.

This is the second part of a two-part paper in which it is demonstrated how these limitations may be overcome; the resulting radiation scheme we refer to is SPARTACUS (the Speedy Algorithm for Radiative Transfer through Cloud Sides). In Part 1, Schäfer *et al.* [2016] addressed shortcomings 1 and 2: they extended the method to the longwave part of the spectrum, for which they found that it was necessary to parameterize aspects of the internal distribution of emitted radiation within a cloud. They also demonstrated that for realistic cloud fields, the use of the exact cloud edge length in SPARTACUS (as computed from high-resolution model fields) tends to lead to an overestimate of longwave 3-D effects, because (a) radiative smoothing means that small-scale cloud structure is not important and (b) clouds tend to cluster together while SPARTACUS assumes a random distribution. They demonstrated that these effects could be accounted for using an *effective cloud edge length*.

In this paper, we address shortcomings 3 and 4. We describe a robust way to solve the modified two-stream equations in which following *Waterman* [1981] and *Flatau and Stephens* [1998], the coupled differential equations are expressed in matrix form leading to a solution in terms of matrix exponentials. This formulation allows inhomogeneity to be represented via the approach of *Shonk and Hogan* [2008]: a partially cloudy layer at a given height is divided into three regions, one clear-sky region and two cloudy regions with different optical depths.

In section 2, the formulation of SPARTACUS is described in the case of shortwave radiation and then in section 3 for longwave radiation. The mathematical symbols used in these sections are defined in the appendix. In section 4 some details are provided of how the method has been implemented to provide an efficient broadband code in combination with a model for gaseous absorption. Then in section 5, SPARTACUS is compared to fully broadband 3-D radiation calculations using the Monte Carlo model "MYSTIC" for a cumulus test case.

2. Shortwave Radiation

2.1. Differential Two-Stream Equations in Matrix Form

In the solar part of the spectrum we consider the radiation field to be split into three streams, diffuse upwelling and downwelling fluxes into a horizontal plane (**u** and **v**, respectively) and the direct downwelling flux into a plane oriented perpendicular to the Sun (**s**). At any given height, these are vectors containing the fluxes in each of m separate regions:

$$\mathbf{u} = \begin{pmatrix} u^a \\ u^b \\ \vdots \end{pmatrix}, \tag{1}$$

and similarly for **v** and **s**. In this section and section 3, all quantities are taken to be for a particular spectral interval. In a traditional representation of clouds in a model, $m = 2$ with superscripts a denoting the clear-sky region and b the cloudy region, but to represent cloud inhomogeneity, *Shonk and Hogan* [2008] proposed the "Tripleclouds" approach with $m = 3$, where b represents optically thin cloud and c optically thick cloud. They found that the radiative effects of cloud inhomogeneity were simulated best if the fractions of the gridbox occupied by regions b and c were the same, i.e., half the cloud fraction. Note that following *Shonk and Hogan* [2008], the m flux components in (1) are defined as the radiative power divided by the area of the *entire gridbox* (not the area of the individual region). Thus, the horizontally averaged flux is found by *summing* the components from each region.

Within a single model layer where the radiative properties of the regions are constant with height, the two-stream equations may be written in matrix form as a set of $3m$ coupled linear ordinary differential equations:

$$\frac{\mathrm{d}}{\mathrm{d}z}\begin{pmatrix} \mathbf{u} \\ \mathbf{v} \\ \mathbf{s} \end{pmatrix} = \mathbf{\Gamma}\begin{pmatrix} \mathbf{u} \\ \mathbf{v} \\ \mathbf{s} \end{pmatrix}, \tag{2}$$

where z is defined as the height measuring downward from zero at the top of this particular layer. (Note that multiple-stream versions of the radiative transfer equation applied to plane-parallel atmospheres may be written in exactly the same form, where the vectors $\mathbf{u}$ and $\mathbf{v}$ would represent m discrete directions rather than m regions.) The matrix $\mathbf{\Gamma}$ describes the interactions between flux components and may be split up into seven component matrices, each of size $m \times m$:

$$\mathbf{\Gamma} = \begin{pmatrix} -\mathbf{\Gamma}_1 & -\mathbf{\Gamma}_2 & -\mathbf{\Gamma}_3 \\ \mathbf{\Gamma}_2 & \mathbf{\Gamma}_1 & \mathbf{\Gamma}_4 \\ & & \mathbf{\Gamma}_0 \end{pmatrix}, \tag{3}$$

where missing entries are taken to contain zeros. The presence of minus signs in front of each matrix on the top line is due to the fact that this line corresponds to upwelling radiation, but the vertical coordinate increases in the downward direction.

Following the form of the two-stream equations presented by *Hogan and Shonk* [2013], the matrices can be seen to have the following forms, showing here the case of $m = 3$. Consider first $\mathbf{\Gamma}_2$, which describes the rate of scattering of diffuse radiation from one direction to the other. Since this scattering occurs entirely within a region, the matrix is diagonal:

$$\mathbf{\Gamma}_2 = \begin{pmatrix} \sigma^a \gamma_2^a & & \\ & \sigma^b \gamma_2^b & \\ & & \sigma^c \gamma_2^c \end{pmatrix}, \tag{4}$$

where σ^j is the extinction coefficient of region j and γ_2 is a function of single-scattering albedo ω and asymmetry factor g. A number of functional forms for γ_2 have been proposed in the literature; see *Meador and Weaver* [1980] and *Zdunkowski et al.* [1980], who also proposed definitions of the quantities γ_1, γ_3, and γ_4, to be introduced shortly. The $\mathbf{\Gamma}_3$ and $\mathbf{\Gamma}_4$ matrices describe the rate at which direct solar radiation is scattered into the upwelling and downwelling diffuse streams, respectively, and are also diagonal:

$$\mathbf{\Gamma}_3 = \begin{pmatrix} \sigma^a \omega^a \gamma_3^a & & \\ & \sigma^b \omega^b \gamma_3^b & \\ & & \sigma^c \omega^c \gamma_3^c \end{pmatrix}, \tag{5}$$

and analogously for $\mathbf{\Gamma}_4$ but using the quantity γ_4.

The remaining two matrices have off-diagonal terms representing lateral transport between regions. The $\mathbf{\Gamma}_0$ matrix describes how direct downwelling fluxes change along their path, while the $\mathbf{\Gamma}_1$ matrix describes how diffuse fluxes change along their path:

$$\mathbf{\Gamma}_0 = \begin{pmatrix} -\sigma^a/\mu_0 - f_{\mathrm{dir}}^{ab} & +f_{\mathrm{dir}}^{ba} & \\ +f_{\mathrm{dir}}^{ab} & -\sigma^b/\mu_0 - f_{\mathrm{dir}}^{ba} - f_{\mathrm{dir}}^{bc} & +f_{\mathrm{dir}}^{cb} \\ & +f_{\mathrm{dir}}^{bc} & -\sigma^c/\mu_0 - f_{\mathrm{dir}}^{cb} \end{pmatrix}, \tag{6}$$

$$\mathbf{\Gamma}_1 = \begin{pmatrix} -\sigma^a \gamma_1^a - f_{\mathrm{diff}}^{ab} & +f_{\mathrm{diff}}^{ba} & \\ +f_{\mathrm{diff}}^{ab} & -\sigma^b \gamma_1^b - f_{\mathrm{diff}}^{ba} - f_{\mathrm{diff}}^{bc} & +f_{\mathrm{diff}}^{cb} \\ & +f_{\mathrm{diff}}^{bc} & -\sigma^c \gamma_1^c - f_{\mathrm{diff}}^{cb} \end{pmatrix}. \tag{7}$$

The $-\sigma/\mu_0$ terms in (6) represent the loss of radiation from the direct stream to either absorption or to scattering into either of the diffuse streams, where μ_0 is the cosine of the solar zenith angle. The $-\sigma\gamma_1$ terms in (7) represent the loss of radiation from a diffuse stream to either absorption or to scattering into the other diffuse stream. The coefficients f_{dir}^{jk} and f_{diff}^{jk} represent the rate at which direct and diffuse radiation, respectively, is transferred from region j to region k. *Hogan and Shonk* [2013] used geometric arguments to show that these coefficients have the form $f^{jk} = L^{jk} \tan\theta / \pi c^k$, where L^{jk} is the length of the interface between regions j and k, per unit area of the gridbox, c^k is the area fraction of region k, and θ is the effective zenith angle of the radiation. For direct shortwave radiation, *Hogan and Shonk* [2013] used the solar zenith angle such that $\tan\theta = \left(1/\mu_0^2 - 1\right)^{1/2}$. However, this neglects the fact that due to delta-Eddington scaling, the so-called "direct" radiation actually includes radiation that has been forward scattered by up to of order 25° in the case of liquid clouds. This means that even for an overhead Sun, there is a chance that direct radiation escapes through a cloud edge. We represent this approximately by using instead $\tan\theta = \left(1/\mu_0^2 - 1 + \theta_{\mathrm{dE}}^2\right)^{1/2}$,

where θ_{dE} is the typical angular deviation (in radians) of direct radiation from the true Sun angle due to delta-Eddington scaling. We find good agreement with Monte Carlo calculations for $\theta_{dE}^2 = 0.06$, i.e., an angle of 14°. In the case of diffuse radiation, Schäfer *et al.* [2016] showed that $\tan\theta = \pi/2$, i.e., $\theta = 57.5°$. Note that for brevity (7) does not show the emissivity-like terms introduced by Schäfer *et al.* [2016] that act as multipliers to the f_{diff}^{jk} terms in the longwave, but they are included in the longwave part of the model. The $\mathbf{\Gamma}_0$ and $\mathbf{\Gamma}_1$ matrices are tridiagonal because it is assumed that there is no contact between regions *a* and *c* (i.e., radiation cannot pass from the optically thick region directly to the clear-sky region without passing through the optically thin region), although there is the option to include this transport in the code.

2.2. Solution to Equations Within One Layer

The formal solution to (2) may be expressed in terms of a matrix exponential [*Waterman*, 1981; *Flatau and Stephens*, 1998]:

$$\begin{pmatrix} \mathbf{u} \\ \mathbf{v} \\ \mathbf{s} \end{pmatrix}_{z=z_1} = \exp(\mathbf{\Gamma} z_1) \begin{pmatrix} \mathbf{u} \\ \mathbf{v} \\ \mathbf{s} \end{pmatrix}_{z=0}. \tag{8}$$

This provides an expression for the fluxes at the base of a layer of thickness z_1 as a function of the fluxes at the top of the layer ($z = 0$), recalling that z is the height measured downward from the top of this individual layer. If 3-D radiative transfer is neglected (i.e., the f_{diff} and f_{dir} terms are set to zero), then the $3m$ equations represented by (2) decouple into m independent sets of three coupled equations, and $\exp(\mathbf{\Gamma} z_1)$ becomes quite sparse with the nonzero entries having analytical forms that are equivalent to the analytical expressions provided by *Meador and Weaver* [1980]. These analytical expressions are used in traditional solutions for the two-stream equations. In the more general case including transport between regions, we need to use a more general approach for computing the matrix exponential, such as the Padé approximation coupled to the scaling and squaring method [*Higham*, 2005]. The squarings may be optimized by exploiting the particular matrix structure: normally, to square a dense $3m \times 3m$ matrix is an O(27 m^3) operation, but the presence of zeros and repeated elements in (3) reduces this to O(11 m^3).

It is convenient to decompose the matrix exponential into seven $m \times m$ component matrices as follows:

$$\exp(\mathbf{\Gamma} z_1) = \begin{pmatrix} \mathbf{E}_{uu} & \mathbf{E}_{uv} & \mathbf{E}_{us} \\ \mathbf{E}_{vu} & \mathbf{E}_{vv} & \mathbf{E}_{vs} \\ & & \mathbf{E}_0 \end{pmatrix}. \tag{9}$$

Thus, for example, $\mathbf{E}_{vs}$ expresses how the downwelling diffuse flux at the base of the layer $\mathbf{v}(z_1)$ depends on the direct flux at the top of the layer $\mathbf{s}(0)$. The zero entries on the bottom row indicate that the direct flux exiting the base of the layer is only a function of the direct flux entering the layer at the top and there is no dependence on the diffuse fluxes, i.e., $\mathbf{s}(z_1) = \mathbf{E}_0\mathbf{s}(0)$. In section 2.3 we show how the direct flux profile can be computed by working down through the atmosphere, accounting for the overlap between regions at each layer interface.

Equations (8) and (9) provide a general solution, but in order to solve for the profile of diffuse fluxes, we really want to work with expressions of the following form (equivalent to *Stephens et al.* [2001, equations 11c and 11d]):

$$\mathbf{u}(0) = \mathbf{T}\mathbf{u}(z_1) + \mathbf{R}\mathbf{v}(0) + \mathbf{S}^+\mathbf{s}(0); \tag{10}$$

$$\mathbf{v}(z_1) = \mathbf{T}\mathbf{v}(0) + \mathbf{R}\mathbf{u}(z_1) + \mathbf{S}^-\mathbf{s}(0), \tag{11}$$

where $\mathbf{T}$ is a matrix representing the transmission of diffuse radiation across the layer, $\mathbf{R}$ is a matrix representing the reflection of diffuse radiation by the layer, and $\mathbf{S}^+$ and $\mathbf{S}^-$ are matrices representing the scattering of radiation from the direct downwelling stream at the top of the layer to the diffuse upwelling stream at the top of the layer and the diffuse downwelling stream at the base of the layer, respectively. Thus, (10) states that the upwelling flux exiting the top of the layer is equal to transmission of the upwelling flux entering the base of the layer plus reflection of the downwelling flux entering the top of the layer plus scattering of the direct solar flux entering the top of the layer and similarly for (11). Figure 1 illustrates the meaning of the elements

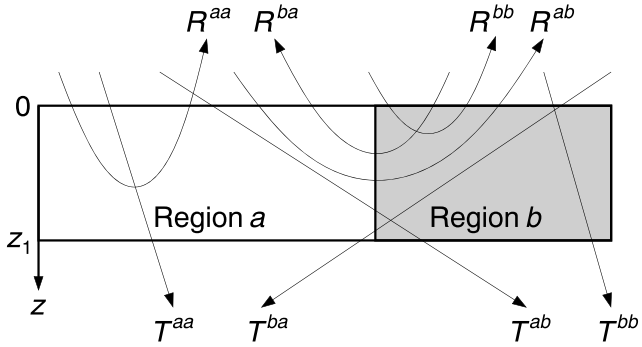

Figure 1. Schematic illustrating the meanings of the elements of the reflectance and transmittance matrices given in (12).

of **T** and **R** for an atmospheric layer containing two regions, in which case

$$\mathbf{T} = \begin{pmatrix} T^{aa} & T^{ba} \\ T^{ab} & T^{bb} \end{pmatrix}, \tag{12}$$

and similarly for the other matrices. In each of the matrices **T**, **R**, $\mathbf{S}^+$, and $\mathbf{S}^-$, off-diagonal elements represent the probability of radiation being transported between regions.

How can we compute these four matrices from (9)? To compute **R**, we consider the case when there is no direct radiation entering the layer from above or diffuse radiation entering from below, i.e., $\mathbf{s}(0) = \mathbf{u}(z_1) = 0_m$ (where 0_m is a vector of length m containing zeros). In this case the first line of (8) becomes $0_m = \mathbf{E}_{uu}\mathbf{u}(0) + \mathbf{E}_{uv}\mathbf{v}(0)$. The reflection matrix for the layer can be thought of as the upwelling fluxes from each region at the top of the layer that emerge as a consequence of a downwelling diffuse flux of unity being applied at the top of the layer independently to each region. Thus, we replace $\mathbf{v}(0)$ by the identity matrix and $\mathbf{u}(0)$ by **R** and rearrange to obtain

$$\mathbf{R} = -\mathbf{E}_{uu}^{-1}\mathbf{E}_{uv}. \tag{13}$$

To compute **T**, consider the second line of (8) in the case that there is no direct radiation entering the layer from above: $\mathbf{v}(z_1) = \mathbf{E}_{vu}\mathbf{u}(0) + \mathbf{E}_{vv}\mathbf{v}(0)$. The transmission by the layer can be found by replacing $\mathbf{v}(0)$ by the identity matrix as before, $\mathbf{v}(z_1)$ by **T** and $\mathbf{u}(0)$ by **R**, and rearranging to get

$$\mathbf{T} = \mathbf{E}_{vu}\mathbf{R} + \mathbf{E}_{vv}. \tag{14}$$

By an analogous procedure we find that the other matrices are

$$\mathbf{S}^+ = -\mathbf{E}_{uu}^{-1}\mathbf{E}_{us}; \tag{15}$$

$$\mathbf{S}^- = \mathbf{E}_{vu}\mathbf{S}^+ + \mathbf{E}_{vs}. \tag{16}$$

2.3. Extension to Multiple Layers

To translate a flux vector from one layer to the next, we need to account for the overlap of each of the regions in one layer with each of the regions in the other layer. *Shonk and Hogan* [2008] defined the *overlap matrix* to describe the overlap of regions in adjacent layers as follows (here shown for $m = 3$):

$$\mathbf{O} = \begin{pmatrix} O^{aa} & O^{ab} & O^{ac} \\ O^{ba} & O^{bb} & O^{bc} \\ O^{ca} & O^{cb} & O^{cc} \end{pmatrix}, \tag{17}$$

where O^{jk} is the fraction of the entire gridbox occupied by region j in the upper layer and region k in the lower layer. Thus, all the elements of the matrix sum to one. *Shonk et al.* [2010] proposed a method to populate the overlap matrix given "overlap parameters" for each of the regions, β^a, β^b, and β^c, such that a value of 1

indicates maximum overlap for that region and a value of 0 represents random overlap. One drawback of their definition of overlap parameter is that total cloud cover is sensitive to all three values, so it is not possible to change the overlap of internal cloud inhomogeneities while keeping cloud boundaries the same. Therefore, we have also implemented a method using the definition of overlap parameter for cloud boundaries, α, of *Hogan and Illingworth* [2000], and a second value α' for internal cloud inhomogeneities. The parameter α' is the correlation coefficient between the cloud internal inhomogeneities in the two layers, but only considering the fraction of the column that is occupied by cloud in both layers. In this case the overlap matrix is

$$\mathbf{O} = \begin{pmatrix} 1-C & \frac{C-c_1}{2} & \frac{C-c_1}{2} \\ \frac{C-c_2}{2} & x(1+\alpha') & x(1-\alpha') \\ \frac{C-c_2}{2} & x(1-\alpha') & x(1+\alpha') \end{pmatrix}, \tag{18}$$

where c_1 and c_2 are the cloud fractions of the upper and lower layers, respectively, and the combined cloud cover of the two layers is $C = \alpha \max(c_1, c_2) + (1-\alpha)(c_1 + c_2 - c_1 c_2)$, and $x = (c_1 + c_2 - C)/4$.

In practice, we want to deal with *directional overlap matrices* **U** and **V** that satisfy

$$\mathbf{u}^{\text{above}} = \mathbf{U}\mathbf{u}^{\text{below}}; \tag{19}$$

$$\mathbf{v}^{\text{below}} = \mathbf{V}\mathbf{v}^{\text{above}}, \tag{20}$$

where $\mathbf{u}^{\text{above}}$ is the upwelling flux just above a layer interface and $\mathbf{u}^{\text{below}}$ is the upwelling flux just below that interface. The matrix **U** is equal to **O** but with each element divided by the sum of the elements in that column (i.e., the cloud fraction in the lower layer), and the matrix **V** is equal to $\mathbf{O}^{\mathrm{T}}$ but again with each element of this transposed matrix divided by the sum of the elements in that column (i.e., the cloud fraction in the upper layer).

The transport of direct solar radiation through the entire atmosphere is then easy to compute. We define $\mathbf{s}^{\text{above}}_{i+1/2}$ and $\mathbf{s}^{\text{below}}_{i+1/2}$ as the direct fluxes just above and below the interface between layers i and $i+1$ (counting down from the top, with the uppermost layer having $i = 1$), as illustrated in Figure 2. If the top-of-atmosphere (TOA) solar flux into a plane perpendicular to the Sun is s_0, then this will be divided into the regions of the uppermost layer according to their fractional coverage:

$$\mathbf{s}^{\text{below}}_{1/2} = s_0 \begin{pmatrix} c_1^a \\ c_1^b \\ c_1^c \end{pmatrix}, \tag{21}$$

for $m = 3$, where c_i^j is the fraction of layer i occupied by region j. The flux exiting the base of layer i is then

$$\mathbf{s}^{\text{above}}_{i+1/2} = \mathbf{E}_{0,i}\mathbf{s}^{\text{below}}_{i-1/2}, \tag{22}$$

which can be translated into the flux entering the top of the layer below via

$$\mathbf{s}^{\text{below}}_{i+1/2} = \mathbf{V}\mathbf{s}^{\text{above}}_{i+1/2}. \tag{23}$$

Repeated application of (22) and (23) yields the profile of direct fluxes all the way down to the surface.

To compute the profile of diffuse fluxes, we use a version of the adding method of *Lacis and Hansen* [1974] in which we proceed up through the atmosphere computing the albedo of the *entire atmosphere* below each layer interface and then proceed down through the atmosphere to compute the fluxes. As discussed by *Shonk and Hogan* [2008], this is also analogous to solving a tridiagonal system of equations by Gaussian elimination followed by back substitution. We define the matrix $\mathbf{A}^{\text{above}}_{i+1/2}$ as the albedo (to diffuse downwelling radiation) of the entire atmosphere (including the surface contribution) below interface $i+1/2$, with the superscript "above" indicating that the elements of **A** are configured for the regions above interface $i+1/2$ (i.e., the regions in layer i rather than $i+1$). We also define the vector $\mathbf{g}^{\text{above}}_{i+1/2}$ as the upwelling fluxes entering into layer i from below that originate from scattering of the direct solar beam below interface $i+1/2$. Thus, we may write

$$\mathbf{u}^{\text{above}}_{i+1/2} = \mathbf{A}^{\text{above}}_{i+1/2}\mathbf{v}^{\text{above}}_{i+1/2} + \mathbf{g}^{\text{above}}_{i+1/2}, \tag{24}$$

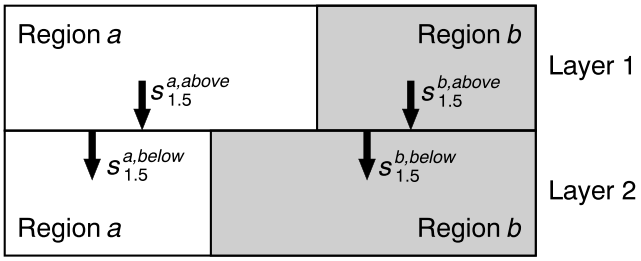

Figure 2. Schematic illustrating the meanings of the direct flux vectors just above and below an interface between layers, $\mathbf{s}^{\text{above}}_{i+1/2}$ and $\mathbf{s}^{\text{below}}_{i+1/2}$. The elements of the vectors correspond to the regions of the layer: $\mathbf{s}^{\text{above}}_{i+1/2} = \left(s^{a,\text{above}}_{i+1/2}, s^{b,\text{above}}_{i+1/2}, \cdots\right)$, with these elements shown in the schematic for the case of two regions and $i = 1$. Equations (22) and (23) show how these flux vectors are computed from each other down through the atmosphere.

i.e., the upwelling diffuse flux just above an interface is equal to the fraction of the downwelling diffuse flux that is reflected upward plus the fraction of the downwelling direct flux that is reflected upward. If the surface albedo to diffuse downwelling radiation is α_{diff}, then the albedo matrix below the lowest atmospheric layer is simply

$$\mathbf{A}^{\text{above}}_{n+1/2} = \alpha_{\text{diff}}\mathbf{I}_m, \tag{25}$$

where n is the number of atmospheric layers. Similarly,

$$\mathbf{g}^{\text{above}}_{n+1/2} = \alpha_{\text{dir}}\mu_0\mathbf{s}^{\text{above}}_{n+1/2}, \tag{26}$$

indicating that a fraction α_{dir} of the direct downward radiation at the surface is reflected back into the same regions. For maximum flexibility we have allowed for the use of different albedos to direct and diffuse downwelling radiation.

We then use the adding method to compute $\mathbf{A}$ and $\mathbf{g}$ just below the interface above, accounting for the possibility of multiple scattering:

$$\mathbf{g}^{\text{below}}_{i-1/2} = \mathbf{q}_{i-1/2} + \mathbf{T}_i\left[\mathbf{I}_m + \mathbf{A}^{\text{above}}_{i+1/2}\mathbf{R}_i + (\mathbf{A}^{\text{above}}_{i+1/2}\mathbf{R}_i)^2 + \cdots\right] \times \left(\mathbf{g}^{\text{above}}_{i+1/2} + \mathbf{A}^{\text{above}}_{i+1/2}\mathbf{p}_{i+1/2}\right), \tag{27}$$

where $\mathbf{q}_{i-1/2} = \mathbf{S}^{+}_i\mathbf{s}^{\text{below}}_{i-1/2}$ is the upwelling diffuse flux at layer interface $i - 1/2$ due to scattering of the direct beam in layer i and $\mathbf{p}_{i+1/2} = \mathbf{S}^{-}_i\mathbf{s}^{\text{below}}_{i-1/2}$ is the downwelling diffuse flux at interface $i + 1/2$ also due to scattering of the direct beam in layer i. Since (27) is a geometric series of matrices, it reduces to

$$\mathbf{g}^{\text{below}}_{i-1/2} = \mathbf{q}_{i-1/2} + \mathbf{T}_i\left(\mathbf{I}_m - \mathbf{A}^{\text{above}}_{i+1/2}\mathbf{R}_i\right)^{-1} \times \left(\mathbf{g}^{\text{above}}_{i+1/2} + \mathbf{A}^{\text{above}}_{i+1/2}\mathbf{p}_{i+1/2}\right).$$

Likewise the albedo matrix just below the interface above is given by

$$\mathbf{A}^{\text{below}}_{i-1/2} = \mathbf{R}_i + \mathbf{T}_i\left(\mathbf{I}_m - \mathbf{A}^{\text{above}}_{i+1/2}\mathbf{R}_i\right)^{-1}\mathbf{A}^{\text{above}}_{i+1/2}\mathbf{T}_i. \tag{28}$$

We then use the directional overlap matrices to convert to values just above the interface:

$$\mathbf{g}^{\text{above}}_{i-1/2} = \mathbf{U}_{i-1/2}\mathbf{g}^{\text{below}}_{i-1/2}, \tag{29}$$

$$\mathbf{A}^{\text{above}}_{i-1/2} = \mathbf{U}_{i-1/2}\mathbf{A}^{\text{below}}_{i-1/2}\mathbf{V}_{i-1/2}. \tag{30}$$

Equations (27)–(30) are applied repeatedly to progress up through the atmosphere. Note that strictly, (30) introduces extra horizontal transport, since it allows downwelling radiation from one region to be reflected back up into another, an effect that is important only in the shortwave. *Shonk and Hogan* [2008] went to some lengths to demonstrate how this transport, which they referred to as "anomalous horizontal transport," could be eliminated to yield better agreement between their Tripleclouds scheme and the Independent Column Approximation. This 3-D transport is not really "anomalous" since it does occur in the real world; for example, direct sunlight from a slant path can illuminate the ground beneath a cloud, and the reflected radiation can

then be intercepted by the cloud. Therefore, we want to represent this transport, and indeed, it appears to be part of the reason that SPARTACUS performs well against fully 3-D simulations, as will be reported in section 5.

We next progress down through the atmosphere to compute the diffuse fluxes. At TOA (layer interface 1/2) we assume no downwelling diffuse flux so $\mathbf{v}_{1/2}^{\text{below}} = 0_m$ and therefore $\mathbf{u}_{1/2}^{\text{below}} = \mathbf{g}_{1/2}^{\text{below}}$. Equations (10) and (11) can be changed to

$$\mathbf{u}_{i+1/2}^{\text{above}} = \mathbf{A}_{i+1/2}^{\text{above}} \mathbf{v}_{i+1/2}^{\text{above}} + \mathbf{g}_{i+1/2}^{\text{above}}; \tag{31}$$

$$\mathbf{v}_{i+1/2}^{\text{above}} = \mathbf{T}_i \mathbf{v}_{i-1/2}^{\text{below}} + \mathbf{R}_i \mathbf{u}_{i+1/2}^{\text{above}} + \mathbf{p}_{i+1/2}. \tag{32}$$

Eliminating $\mathbf{u}_{i+1/2}^{\text{above}}$ yields

$$\mathbf{v}_{i+1/2}^{\text{above}} = \left(\mathbf{I}_m - \mathbf{R}_i \mathbf{A}_{i+1/2}^{\text{above}}\right)^{-1} \times \left(\mathbf{T}_i \mathbf{v}_{i-1/2}^{\text{below}} + \mathbf{R}_i \mathbf{g}_{i+1/2}^{\text{above}} + \mathbf{p}_{i+1/2}\right). \tag{33}$$

Thus, application of (33) followed by (31) provides the fluxes just above the interface below. Equation (20) is then applied to obtain $\mathbf{v}_{i+1/2}^{\text{below}}$, and the procedure is repeated to obtain the flux profile down through the atmosphere.

3. Longwave Radiation

In the longwave part of the spectrum we include scattering, so we take a similar approach in modifying the two-stream equations but need to modify (2) to remove the direct solar beam and to add thermal emission:

$$\frac{\mathrm{d}}{\mathrm{d}z}\begin{pmatrix}\mathbf{u}\\ \mathbf{v}\end{pmatrix} = \mathbf{\Gamma}\begin{pmatrix}\mathbf{u}\\ \mathbf{v}\end{pmatrix} + \begin{pmatrix}-\mathbf{b}_0\\ \mathbf{b}_0\end{pmatrix} + \begin{pmatrix}-\mathbf{b}'\\ \mathbf{b}'\end{pmatrix} z, \tag{34}$$

where now

$$\mathbf{\Gamma} = \begin{pmatrix}-\mathbf{\Gamma}_1 & -\mathbf{\Gamma}_2\\ \mathbf{\Gamma}_2 & \mathbf{\Gamma}_1\end{pmatrix}, \tag{35}$$

with $\mathbf{b}_0$ representing the rate of emission into each region at $z = 0$ and $\mathbf{b}'$ its rate of change with z. Since thermal emission is isotropic, the same terms are used for the upwelling and downwelling emission, but with a minus sign for the upwelling component since the height variable z increases in a downward direction. For atmospheric layer i,

$$\mathbf{b}_0 = D\pi B(T_{i-1/2}) \begin{pmatrix} c_i^a \sigma_i^a (1-\omega_i^a) \\ c_i^b \sigma_i^b (1-\omega_i^b) \\ c_i^c \sigma_i^c (1-\omega_i^c) \end{pmatrix}, \tag{36}$$

and

$$\mathbf{b}' = D\pi \frac{B(T_{i+1/2}) - B(T_{i-1/2})}{z_1} \begin{pmatrix} c_i^a \sigma_i^a (1-\omega_i^a) \\ c_i^b \sigma_i^b (1-\omega_i^b) \\ c_i^c \sigma_i^c (1-\omega_i^c) \end{pmatrix}, \tag{37}$$

where $D = 1.66$ is the diffusivity factor appropriate for thermal radiation [e.g., *Fu et al.*, 1997] and $B(T_{i-1/2})$ is the Planck function at the temperature at interface $i - 1/2$ in the spectral interval being simulated. Here we have assumed the Planck emission to vary linearly with height; since the definition of $\mathbf{\Gamma}$ contains extinction σ that is treated as constant with height, this assumption is equivalent to the common assumption that the Planck function varies linearly with optical depth.

The solution to (34) is

$$\begin{pmatrix}\mathbf{u}\\ \mathbf{v}\end{pmatrix}_{z=z_1} = \exp(\mathbf{\Gamma} z_1)\begin{pmatrix}\mathbf{u}\\ \mathbf{v}\end{pmatrix}_{z=0} + \left[\mathbf{I}_{2m} - \exp(\mathbf{\Gamma} z_1)\right]\begin{pmatrix}\mathbf{c}_0\\ \mathbf{d}_0\end{pmatrix} + \begin{pmatrix}\mathbf{c}'\\ \mathbf{d}'\end{pmatrix} z_1, \tag{38}$$

where

$$\begin{pmatrix}\mathbf{c}'\\ \mathbf{d}'\end{pmatrix} = -\mathbf{\Gamma}^{-1}\begin{pmatrix}-\mathbf{b}'\\ \mathbf{b}'\end{pmatrix}; \begin{pmatrix}\mathbf{c}_0\\ \mathbf{d}_0\end{pmatrix} = \mathbf{\Gamma}^{-1}\begin{pmatrix}\mathbf{c}' + \mathbf{b}_0\\ \mathbf{d}' - \mathbf{b}_0\end{pmatrix}. \tag{39}$$

As in (9), we can decompose the matrix exponential into

$$\exp(\mathbf{\Gamma} z_1) = \begin{pmatrix} \mathbf{E}_{uu} & \mathbf{E}_{uv} \\ \mathbf{E}_{vu} & \mathbf{E}_{vv} \end{pmatrix}. \tag{40}$$

Thus, the reflection, transmission, and albedo matrices may be computed using the same equations (13), (14), (25), and (28) as in the shortwave case. The $\mathbf{g}_{i+1/2}$ vector introduced in (24), however, is different in that it now represents emission by the entire atmosphere below interface $i + 1/2$, rather than scattering by the direct solar beam. At the base of the lowest model layer it is simply the emission by the surface multiplied by the fraction of each region, i.e., for $m = 3$

$$\mathbf{g}_{n+1/2} = \pi \epsilon B(T_s) \begin{pmatrix} c_n^a \\ c_n^b \\ c_n^c \end{pmatrix}, \tag{41}$$

where ϵ is the surface emissivity and $B(T_s)$ is the Planck function at surface temperature T_s in the spectral interval being simulated. To obtain $\mathbf{g}$ at other heights, we need first to calculate $\mathbf{q}$, the upwelling flux at the top of the layer due to emission within it, and $\mathbf{p}$, the downwelling flux at the base of the layer due to emission within it. Consider the case when there is no diffuse radiation entering the radiation from the top or the bottom, i.e., $\mathbf{v}(0) = \mathbf{u}(z_1) = 0_m$. Equation (38) then becomes $0 = \mathbf{E}_{uu}\mathbf{u}(0) + (\mathbf{I} - \mathbf{E}_{uu})\mathbf{c}_0 + \mathbf{c}' z_1 - \mathbf{E}_{uv}\mathbf{d}_0$ and $\mathbf{v}(z_1) = \mathbf{E}_{vu}\mathbf{u}(0) - \mathbf{E}_{vu}\mathbf{c}_0 + (\mathbf{I} - \mathbf{E}_{vv})\mathbf{d}_0 + \mathbf{d}' z_1$. Recognizing that in this case $\mathbf{q} = \mathbf{u}(0)$ and $\mathbf{p} = \mathbf{v}(z_1)$, we have

$$\mathbf{q} = \mathbf{c}_0 - \mathbf{E}_{uu}^{-1}\left(\mathbf{c}_0 + \mathbf{c}' z_1 - \mathbf{E}_{uv}\mathbf{d}_0\right); \tag{42}$$

$$\mathbf{p} = \mathbf{E}_{vu}(\mathbf{q} - \mathbf{c}_0) + (\mathbf{I}_m - \mathbf{E}_{vv})\mathbf{d}_0 + \mathbf{d}' z_1. \tag{43}$$

We may then use (27) and (29) to compute the profile of $\mathbf{g}$ up through the atmosphere, followed by the downward pass to compute fluxes as in the shortwave case.

4. Implementation Details

The algorithm described in this paper, as well as the longwave-specific features developed in Part 1, has been coded up in a form suitable for use both offline and incorporated into European Centre for Medium-Range Weather Forecasts' (ECMWF) numerical model of the atmosphere. The overarching design goal has been to keep the code as modular as possible, such that the following four components of the code may be changed independently: (a) gas optics model, (b) cloud optics model, (c) aerosol optics model, and (d) solver.

Currently, the gas optics model is the Rapid Radiative Transfer Model for General Circulation Models (RRTM-G) [*Mlawer et al.*, 1997], as implemented in the ECMWF forecast model [*Morcrette et al.*, 2008]. It is the gas optics model that determines the number of pseudo-monochromatic calculations required for the full spectrum. RRTM-G uses a correlated-*k* distribution method to represent the absorption by 10 atmospheric gases. It divides the longwave spectrum into 16 intervals within which a total of 140 pseudo-monochromatic calculations are performed and the shortwave into 14 bands within which a total of 112 pseudo-monochromatic calculations are performed. The liquid cloud optical properties use a Padé-approximant fitted to Mie calculations for each of the 30 spectral bands of RRTM-G, computed using code from the Met Office's "SOCRATES" (Suite of Community Radiative Transfer codes based on Edwards and Slingo) radiation package (J. Manners, personal communication, 2014). Various options are available for representing ice and aerosol optical properties, but since neither ice clouds nor aerosols are included in any of the simulations in this paper, they are not discussed here. Finally, the solver is the SPARTACUS model as described in this paper, but with the option to turn 3-D effects off in which case it reduces to a Tripleclouds solver [*Shonk and Hogan*, 2008] if three regions are used or a more traditional scheme similar to that of *Edwards and Slingo* [1996] if two regions are used. Turning off 3-D effects speeds up the scheme by a factor of 2–3, depending on the amount of cloud in the profile. An implementation of the Monte Carlo Independent Column Approximation (McICA) [*Pincus et al.*, 2003] is also available; this solver obviously does not represent 3-D effects.

Cloud inhomogeneity is described by the fractional standard deviation (FSD) of in-cloud optical depth or water content, i.e., the standard deviation divided by the mean. Various observational studies have reported values of this variable for different cloud types [*Shonk et al.*, 2010; *Hill et al.*, 2015]. If FSD is small, then the

in-cloud mean optical depth or water content can be scaled by $x^b = 1 - \mathrm{FSD}$ to get the value for the optically thinner cloudy region (region *b*) and $x^c = 1 + \mathrm{FSD}$ for the optically thicker cloudy region (region *c*), but this is unphysical for FSD > 1. Therefore, we follow the result of *Shonk and Hogan* [2008] that region *b* should use the 16th percentile of the distribution. We assume a lognormal distribution, for which it can be shown that the 16th percentile is found by using

$$x^b = (\mathrm{FSD}^2 + 1)^{-1/2} \exp\left\{ -\left[\ln(\mathrm{FSD}^2 + 1)\right]^{1/2} \right\}, \tag{44}$$

which is in the range 0 to 1 for any value of FSD. The in-cloud mean optical depth or water content is conserved by then using $x^c = 2 - x^b$.

In solving the two-stream equations in a single layer, the matrix exponential method is more expensive than implementing the equations of *Meador and Weaver* [1980]. Therefore, the algorithm reverts to using *Meador and Weaver* [1980] in layers when 3-D effects would be very small or zero, such as in completely clear or overcast layers, and for spectral intervals when the optical depth of gases in an individual layer exceeds 8. Comparisons confirm that when 3-D transport is neglected, the matrix exponential method and the *Meador and Weaver* [1980] equations produce virtually identical solutions.

Preliminary experiments with the 3-D SPARTACUS radiation scheme in the ECMWF model show the scheme to be around 3.5 times more computationally expensive than the existing McICA scheme [*Morcrette et al.*, 2008] in which 3-D effects are ignored. The existing scheme uses exactly the same number of spectral intervals as SPARTACUS, but with a traditional two-stream plane-parallel solver in each shortwave interval and a simpler no-scattering solver in each longwave interval. Since the existing scheme accounts for only 5–10% of the total cost of the model, SPARTACUS is a viable candidate for a future operational configuration, although further work to optimize the matrix exponential calculations and other matrix operations is clearly needed.

5. Comparison With Full Broadband 3-D Radiation Calculations

5.1. Overview

The broadband version of SPARTACUS has been evaluated by comparing to fully 3-D calculations with the library for radiative transfer "libRadtran" [*Mayer and Kylling*, 2005], using the 3-D MYSTIC solver (Monte Carlo code for the physically correct tracing of photons in cloudy atmospheres) by *Mayer* [2009]. The RRTM-G gas absorption model is currently not implemented in libRadtran, so instead, it used the 32-band correlated-*k* distribution model of *Kato et al.* [1999] in the shortwave and the 12-band model of *Fu and Liou* [1992] in the longwave. The heating rate simulations with MYSTIC in the longwave part of the spectrum follow the methods described by *Klinger and Mayer* [2014].

The scene used for comparison was the 3-D large-eddy simulation of cumulus clouds used by *Cahalan et al.* [2005], also used in Part 1, in which clouds were described by their liquid water content and effective radius in a periodic domain measuring 6.4 km in each horizontal dimension with a resolution of 67 m in the horizontal and 40 m in the vertical. The cloud field was embedded in the midlatitude summer standard atmosphere over a surface with a shortwave albedo of 0.08 and a longwave emissivity of 0.98. The surface skin temperature was 21°C, and the cloud base temperature was 16°C. Aerosols were not included.

The profile of cloud descriptors required by SPARTACUS was computed from the 3-D scene: cloud fraction and horizontal mean water content (Figures 3a and 3b) were computed in the usual way, while droplet effective radius was computed as the water content-weighted mean. To represent cloud inhomogeneity, SPARTACUS requires the fractional standard deviation of in-cloud water content, which is simply the standard deviation of in-cloud water content divided by the in-cloud mean (Figure 3c). To represent lateral transport, SPARTACUS requires the cloud edge length per unit area of the gridbox, L^{ab}. It was found in Part 1 that a good approximation for the "radiatively effective" cloud edge length of a cloud field is found by fitting an ellipse to each cloud at each height. A more physically intuitive variable is the "effective cloud diameter" [*Jensen et al.*, 2008], defined as the diameter of identical circular clouds that have the same value of L^{ab} and cloud fraction as the original field; this is plotted in Figure 3d and is defined as

$$C_D = 4c/L^{ab}, \tag{45}$$

where *c* is the cloud fraction. In Part 1 it was shown that the effect of cloud clustering for this cloud field could be represented approximately in the longwave by scaling L^{ab} by a factor of 0.69, equivalent to dividing C_D by the same value; this is shown by the dashed line in Figure 3d.

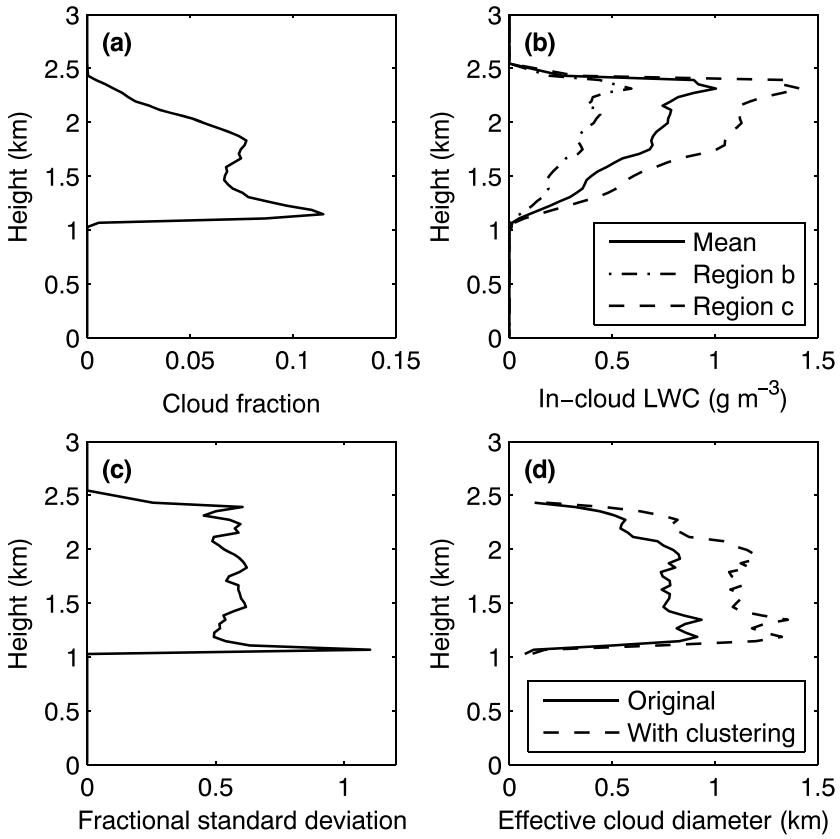

Figure 3. Profiles of cloud properties from the cumulus test case used as input to SPARTACUS: (a) cloud fraction, (b) mean in-cloud liquid water content and the values used in the two cloudy regions *b* and *c*, (c) fractional standard deviation of in-cloud liquid water content, and (d) effective cloud diameter, both the original values computed from ellipses fitted to the clouds in each layer and applying a scaling to approximately represent cloud clustering on longwave radiative transfer.

The overlap parameter α was computed for each adjacent pair of layers in the 3-D scene via the overlap matrix described in section 2.3. When the overlap rules used by SPARTACUS were applied to this α profile, the total cloud cover was computed to be 0.258, higher than the true value for the scene of 0.234. This would be expected to lead to errors in the SPARTACUS calculation that are not due to 3-D effects. If the overlap decorrelation length corresponding to each α value is increased by 26%, then applying the overlap rules to the new α profile yields the true cloud cover. However, this does not preserve the true overlap of clouds in adjacent layers, which is also important for 3-D transport. In this situation it is not clear how best to construct an input profile for SPARTACUS that will lead to the fairest comparison with fully 3-D radiation calculations. Therefore, we make a compromise and scale the overlap decorrelation length by the halfway value of 13% to yield the profile of α to be used as input to SPARTACUS.

Experiments are performed in which lateral transport is both included (3-D) and excluded (1-D or ICA). In the 1-D case, libRadtran uses the six-stream DISORT solver (discrete ordinates radiative transfer program for a multilayered plane-parallel medium) [see *Buras et al.*, 2011] and the Independent Column Approximation (ICA). DISORT has been found to provide almost identical results to MYSTIC in 1-D, but at much lower computational cost. In the 3-D shortwave experiment, MYSTIC is run four times with different solar azimuth angles to estimate the instantaneous uncertainty due to the particular orientation of the cloud field with respect to the incoming solar beam. SPARTACUS assumes a random cloud distribution such that it effectively averages over all possible azimuthal orientations of the Sun with respect to the cloud field. No account is made in either model for the curvature of the Earth.

As mentioned in the context of (30), SPARTACUS does include what *Shonk and Hogan* [2008] called anomalous horizontal transport even when 3-D effects are "turned off" by setting the *f* terms in (6) and (7) to zero. While this inclusion of some horizontal transport actually makes the 1-D simulations a little bit more realistic with

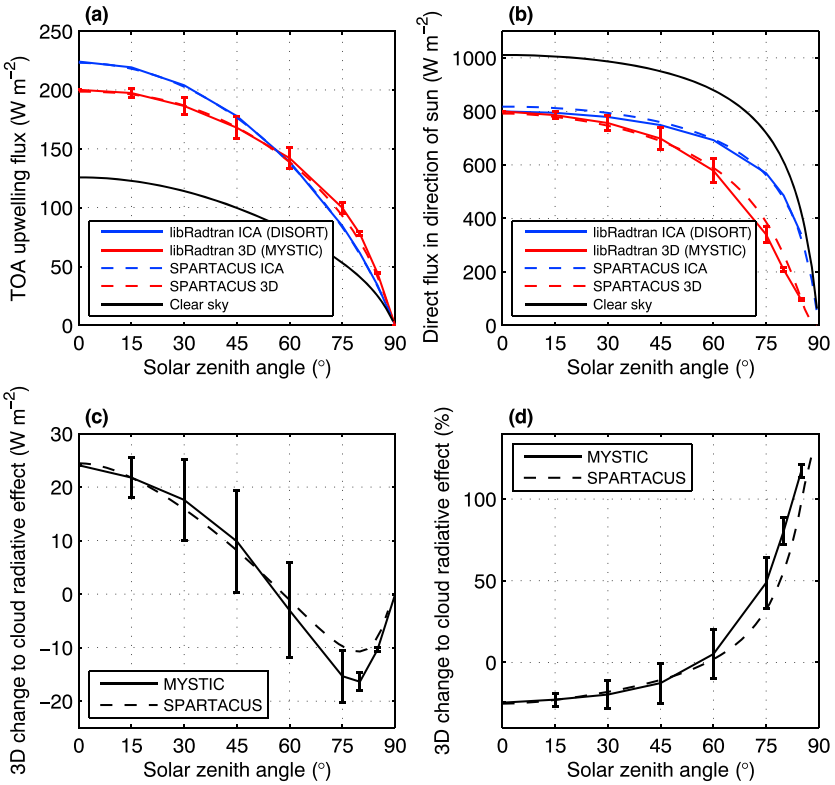

Figure 4. Comparison of simulated broad shortwave fluxes from libRadtran (using the MYSTIC Monte Carlo solver for 3-D calculations) and SPARTACUS for the I3RC cumulus test case versus solar zenith angle. (a) Top-of-atmosphere (TOA) upwelling fluxes for the two models both including lateral transport (3-D) and excluding it (ICA), along with values for clear skies. (b) As in Figure 4a but comparing the direct component of surface solar flux into a plane perpendicular to the Sun. (d) The change to TOA cloud radiative effect due to the inclusion of 3-D effects. (d) As in Figure 4c but as a percentage. The MYSTIC 3-D results are the average over four calculations with the solar azimuth angle 90° apart, and the error bars in each panel represent the standard deviation of these four simulations.

respect to fully 3-D radiation calculations, it does lead to poorer agreement with the Independent Column Approximation in the shortwave. Therefore, a more suitable SPARTACUS shortwave reference case in which 3-D effects are excluded is obtained by running it in ICA mode, i.e., on each individual column of the original cloud field as is done with libRadtran.

5.2. Shortwave

Figure 4a compares the TOA-reflected shortwave flux between libRadtran and SPARTACUS versus solar zenith angle θ_0. In general, the agreement is very good in both the ICA and 3-D experiments. To examine the differences in more detail, it is helpful to calculate the TOA cloud radiative effect (CRE), defined as the net TOA flux (downwelling minus upwelling) for cloudy sky conditions minus that for the equivalent clear-sky profile. Over most surfaces this is a negative quantity in the shortwave. Figures 4c and 4d depict the change to CRE when 3-D effects are introduced in absolute and percentage units, respectively. SPARTACUS is able to capture both the increase in the magnitude of CRE when the Sun is low in the sky due to interception of the direct solar beam by cloud sides and the reduction in the magnitude of CRE when the Sun is high in the sky due to some forward scattered radiation escaping from cloud edges. These mechanisms were discussed further by *Várnai and Davies* [1999] and *Hogan and Shonk* [2013].

The largest errors in the SPARTACUS 3-D calculations are at $\theta_0 \simeq 75°$ where SPARTACUS underestimates reflected flux (and correspondingly overestimates CRE) by 5.6 W m^{-2}. Nonetheless, the strong difference between the ICA and 3-D reflectances, which exceed 20 W m^{-2} for some solar zenith angles, has been captured well by SPARTACUS, and the error compared to MYSTIC is typically of the same order or less than the spread of MYSTIC results for different solar azimuth angles (represented by the error bars). See Table 1 for the values of CRE at two contrasting solar zenith angles.

Table 1. Cloud Radiative Effect (CRE) Simulated by Libradtran and SPARTACUS for the Cumulus Cloud Field Discussed in Section 5.1, Specifically the Top-of-Atmosphere (TOA) Shortwave CRE at Solar Zenith Angles of 0° and 75°, and the Longwave CRE at Both Surface and TOA[a]

Spectral Region/Location	Model	1-D CRE (W m^{-2})	3-D Effect (W m^{-2})	3-D Effect (%)
Shortwave TOA (0°)	libRadtran	−98.1	+24.1	−25%
	SPARTACUS	−97.3	+24.5	−25%
Shortwave TOA (75°)	libRadtran	−31.5	−15.3	+49%
	SPARTACUS	−30.1	−9.7	+32%
Longwave surface	libRadtran	13.1	3.8	29%
	SPARTACUS	14.1	4.6 (6.3)	32% (45%)
Longwave TOA	libRadtran	2.9	0.25	9%
	SPARTACUS	2.8	0.39 (0.69)	14% (25%)

[a]The first column of numbers gives CRE when 3-D effects are neglected ("1D"), while the remaining columns give the change to CRE when 3-D effects are included, in W m^{-2} and %. The longwave 3-D effects for SPARTACUS are computed after the radiatively effective cloud edge length has been multiplied by a factor of 0.69 to approximately represent the effects of cloud clustering; the numbers in parentheses indicate the results when this effect has not been accounted for.

In Part 1 it was found that for capturing 3-D effects in the longwave it was necessary to account for cloud clustering by scaling down the cloud edge length. If this is done in the shortwave, then it actually makes the comparison to MYSTIC somewhat worse; specifically, the TOA-reflected flux is reduced by 4.5 W m^{-2} for θ_0 between 60° and 75°, increasing the existing bias in SPARTACUS for this range of solar zenith angle. The fact that it appears not to be necessary to account for clustering in the shortwave is presumably related to differences between the way that direct and diffuse radiation lead to 3-D effects; the 3-D effect in the shortwave is mostly associated with the behavior of direct solar radiation, while in the longwave all radiation is diffuse. However, further investigations would be required for a fuller understanding.

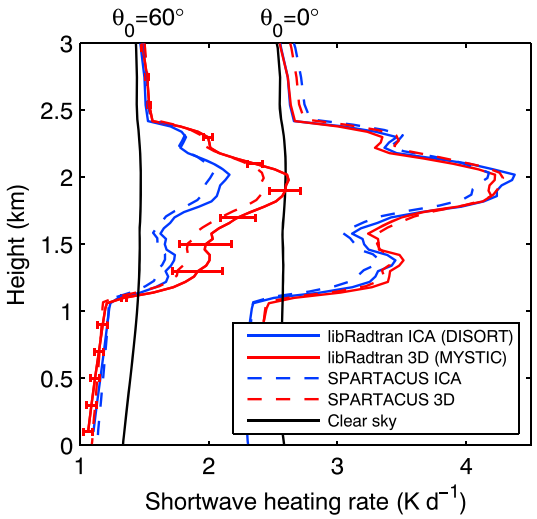

Figure 5. Comparison of broadband shortwave heating rate profile between libRadtran and SPARTACUS, for the I3RC cumulus test case. Two groups of lines are presented, corresponding to solar zenith angles of $\theta_0 = 0°$ and 60°, as indicated at the top of the figure. Results are shown from both schemes in the ICA case neglecting 3-D transport (blue lines) and including 3-D transport (red lines). The clear-sky values from each scheme are indistinguishable, so only one line is shown for each θ_0. The error bars on the MYSTIC line for $\theta_0 = 60°$ represent the standard deviation of the calculations for the four different solar azimuth angles.

Figure 4b depicts the direct component of the surface solar flux measured into a plane perpendicular to the Sun. This quantity is of particular interest for the solar energy industry when estimating the yield by photovoltaic cells mounted on solar trackers. The increased probability of the direct beam being intercepted by cloud sides is represented by the 3-D simulations, which drop below the ICA values to an increasing degree as solar zenith angle is increased. The 3-D version of SPARTACUS agrees particularly well with MYSTIC, suggesting that SPARTACUS could be used to forecast the yield by photovoltaic cells better than existing 1-D schemes.

Figure 5 compares shortwave atmospheric heating rate profiles at two solar zenith angles. For overhead Sun, 3-D transport has a weak effect on heating rate, while for a solar zenith angle of 60°, the enhanced interception of direct solar radiation leads to larger heating than the 1-D equivalent. SPARTACUS captures most of this difference, although there is some underestimation of the 3-D effect. Note that the values here are horizontal averages across the clear and cloudy regions of the gridbox, and since the cloud fraction is only around 0.075, the *in-cloud* heating rates are much larger than shown here.

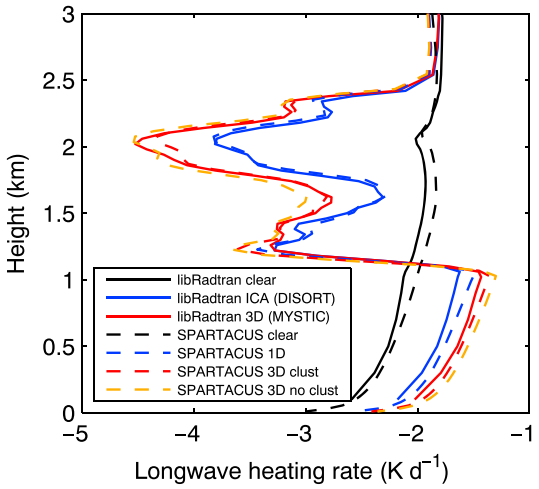

Figure 6. Comparison of broadband longwave heating rate profile between libRadtran (using the MYSTIC Monte Carlo solver for 3-D calculations) and SPARTACUS, for the I3RC cumulus test case. Results are shown from both models in clear skies (black lines), the 1-D case neglecting 3-D transport (blue lines) and including 3-D transport (red lines). The SPARTACUS 3-D "clust" line has had its edge length reduced to account for the effect of cloud clustering, whereas the dashed orange line shows the heating rate if this adjustment is not performed.

5.3. Longwave

Figure 6 compares the horizontal mean broadband longwave heating rates between MYSTIC and SPARTACUS. Considering first the case when 3-D effects are neglected (blue lines), the agreement is good, particularly in the cloud layer. The difference below cloud is also seen in the clear-sky profile and is believed to be predominantly due to the different gas absorption models used.

Two SPARTACUS simulations are shown including 3-D effects. Both use as a starting point the radiatively effective cloud edge length, computed by fitting ellipses to the clouds in each layer (described in Part 1). By default, SPARTACUS assumes that clouds are randomly distributed, but if there is some clustering, then in reality, diffuse radiation emitted from the side of a cloud is more likely to be absorbed by another cloud rather than escaping out of the cloudy layers, compared to a random distribution. The red dashed line incorporates the empirical finding of Part 1 (for the same cloud field) that this effect can be represented approximately by multiplying the edge length by 0.69, while the orange dashed line does not perform this scaling. The difference in terms of heating rates is actually rather small: reducing edge length does indeed reduce the cooling rate, but both lines fit the MYSTIC profile quite well. Indeed, even if the effects of clustering are neglected, SPARTACUS provides a much better estimate of longwave atmospheric heating than the equivalent 1-D calculation. As discussed in Part 1, there is no reason to believe that this 0.69 factor is universal so further work is required to characterize this factor, and its uncertainty, for a wider range of cloud fields.

Table 1 shows the change to longwave CRE due to 3-D transport at both the surface and TOA. The change is far larger at the surface, principally because cumulus clouds have a much larger CRE at the surface (and for predicting surface temperature on weather or climate timescales it is of course surface fluxes that are most relevant). The MYSTIC simulation shows that 3-D effects increase the surface CRE of this cumulus field by around 30%, the same value as found by *Heidinger and Cox* [1996] from both observations and modeling. When clustering is accounted for, SPARTACUS matches this value closely in percentage terms, but if the clouds are assumed to be distributed randomly, then the estimate of the 3-D enhancement of 45% is too high. We stress that this is not an independent test of the clustering factor proposed in Part 1, since this is the same cloud field apart from the addition of atmospheric gases and cloud horizontal structure. However, it does indicate that simple manipulation of cloud edge length may be sufficient to represent the impact of clustering on both heating rate profiles and surface fluxes.

6. Conclusions

This paper has described the development of the first broadband radiation scheme that is capable of representing 3-D effects in both the shortwave and the longwave and yet is fast enough to be considered for use in weather and climate models. This work follows from the original idea to modify the two-stream equations to represent lateral transport presented by *Hogan and Shonk* [2013], which was extended to the longwave in Part 1. Here we have shown that expressing the equations in matrix form and solving them using matrix exponentials yields a much more elegant and accurate scheme compared to the solution method proposed by *Hogan and Shonk* [2013].

Broadband comparisons with Monte Carlo calculations for a cumulus test case have demonstrated that SPARTACUS can represent 3-D effects in both the longwave and shortwave with good accuracy, when the variables describing cloud structure are available. In particular, the fitting of ellipses to the clouds in each layer of the

model was found to be essential to estimating the radiatively effective cloud edge length, as described in Part 1.

There are a few aspects of the formulation of SPARTACUS that would benefit from further investigation, the most obvious being the representation of cloud clustering. More high-resolution cloud fields will need to be studied to characterize clustering behavior and possibly to come up with a more physically based representation of it in SPARTACUS than simply scaling down the cloud edge length. It would also be useful to understand why it appears to be necessary to represent clustering only in the longwave. Nonetheless, it should be stressed that in both the longwave and the shortwave, the changes to fluxes and heating rates when 3-D effects are introduced are considerably larger than the additional changes when clustering is accounted for.

In a future paper we will report results from global model simulation with SPARTACUS, to estimate the importance of 3-D effects on the radiation balance at a global scale and indeed whether this feeds back on the cloud distribution. This will require a parameterization of cloud edge length for the cloud types represented in the model, which could be based on a combination of cloud-resolving model output [e.g., *Neggers et al.*, 2003], satellite observations [e.g., *Jensen et al.*, 2008], and radar observations of 3-D cloud structure [e.g., *Fielding et al.*, 2014; *Stein et al.*, 2015].

Appendix A: List of Symbols

The following list includes symbols used in more than one equation and therefore not always defined in their immediate context in the text.

- 0_m column vector of length m containing zeros.
- $\mathbf{A}_{i+1/2}^{\text{above}}$ diffuse albedo of entire atmosphere below interface $i + 1/2$, with matrix elements configured for regions in layer *above* interface.
- $\mathbf{b}_0$ rate of thermal emission into each region at top of layer.
- $\mathbf{b}'$ rate of change of thermal emission with z.
- c_i^j fraction of layer i occupied by region j.
- c_i cloud fraction in layer i, such that $c_i = c_i^2 + c_i^3$.
- $\mathbf{E}_0$ transmission matrix for direct radiation.
- $\mathbf{E}_{jk}$ component of matrix exponential expressing relationship between flux component j at layer top to k at layer base.
- $f_{\text{dir}}^{jk}, f_{\text{diff}}^{jk}$ rate of transport of direct and diffuse radiation from region j to k.
- $\mathbf{g}_{i+1/2}^{\text{above}}$ upwelling fluxes entering into each region of layer i from below that originate from scattering of direct solar beam, or thermal emission, below interface $i + 1/2$.
- $\mathbf{I}_n$ identity matrix of size $n \times n$.
- L^{jk} length of interface between regions j and k, per unit area of gridbox.
- $\mathbf{O}$ matrix describing how regions in adjacent layers are overlapped.
- $\mathbf{q}_{i-1/2}$ upwelling flux at interface $i - 1/2$ due to scattering of direct beam, or thermal emission, in each region of layer i.
- $\mathbf{p}_{i+1/2}$ downwelling diffuse flux at interface $i+1/2$ due to scattering of the direct beam, or thermal emission, in each region of layer i.
- $\mathbf{R}_i$ diffuse reflection matrix of layer i.
- $\mathbf{s}_{i+1/2}^{\text{above}}$ direct solar flux in each region just above interface $i + 1/2$.
- $\mathbf{S}_i^+$ matrix describing the fraction of direct solar radiation entering each region at the top of layer i that is scattered back up out of each region
- $\mathbf{S}_i^-$ Matrix describing the fraction of direct solar radiation entering each region at the top of layer i that is scattered out of each region at the base of that layer.
- $\mathbf{T}_i$ diffuse transmission matrix of layer i.
- $\mathbf{u}_{i+1/2}^{\text{above}}$ upwelling flux in each region just above interface $i + 1/2$.
- $\mathbf{U}_{i+1/2}$ upward overlap matrix expressing how upwelling fluxes in each region just below interface $i + 1/2$ are transported into the regions just above this interface.
- $\mathbf{v}_{i+1/2}^{\text{above}}$ downwelling flux in each region just above interface $i + 1/2$.
- $\mathbf{V}_{i+1/2}$ downward overlap matrix expressing how downwelling fluxes in each region just above interface $i + 1/2$ are transported into the regions just below this interface.
- z height measured downward from top of a layer.

z_1 thickness of a layer.
α, α' overlap parameter of cloud boundaries and cloud internal inhomogeneities, respectively.
$\alpha_{\mathrm{dir}}, \alpha_{\mathrm{diff}}$ surface albedo to direct and diffuse radiation.
$\gamma_1^j \cdots \gamma_4^j$ two-stream coefficients in region j.
$\mathbf{\Gamma}$ matrix describing interactions between flux components in two-stream equations.
$\mathbf{\Gamma}_0 \cdots \mathbf{\Gamma}_4$ submatrices of $\mathbf{\Gamma}$ representing specific interactions.
μ_0 cosine of solar zenith angle.
σ^j, ω^j extinction coefficient and single-scattering albedo of region j.

Acknowledgments
The second author was supported by a doctoral studentship from the EU-funded "ITaRS" project. We thank Susanne Crewell for her valuable discussions throughout the course of this work. James Manners is thanked for his assistance in using the SOCRATES code for parameterizing droplet scattering properties. The data used in this paper are available on request from the corresponding author.

References

Barker, H. W., J. N. S. Cole, J. Li, B. Yi, and P. Yang (2015), Estimation of errors in two-stream approximations of the solar radiative transfer equation for cloudy-sky conditions, *J. Atmos. Sci.*, *72*, 4053–4074.

Buras, R., T. Dowling, and C. Emde (2011), New secondary-scattering correction in DISORT with increased efficiency for forward scattering, *J. Quant. Spectrosc. Radiat. Transfer*, *112*, 2028–2034.

Cahalan, R. F., et al. (2005), The I3RC: Bringing together the most advanced radiative transfer tools for cloudy atmospheres, *Bull. Am. Meteorol. Soc.*, *86*, 1275–1293.

Edwards, J. M., and A. Slingo (1996), Studies with a flexible new radiation code. 1: Choosing a configuration for a large-scale model, *Q. J. R. Meteorol. Soc.*, *122*, 689–719.

Fielding, M. D., J. C. Chiu, R. J. Hogan, and G. Feingold (2014), A novel ensemble method for retrieving properties of warm cloud in 3-D using ground-based scanning radar and zenith radiances, *J. Geophys. Res. Atmos.*, *119*, 10,912–10,930, doi:10.1002/2014JD021742.

Flatau, P. J., and G. L. Stephens (1998), On the fundamental solution of the radiative transfer equation, *J. Geophys. Res.*, *93*, 11,037–11,050.

Fu, Q., and K. N. Liou (1992), On the correlated *k*-distribution method for radiative transfer in nonhomogeneous atmospheres, *J. Atmos. Sci.*, *49*, 2139–2156.

Fu, Q., K. N. Liou, M. C. Cribb, T. P. Charlock, and A. Grossman (1997), Multiple scattering parameterization in thermal infrared radiative transfer, *J. Atmos. Sci.*, *54*, 2799–2812.

Heidinger, A. K., and S. K. Cox (1996), Finite-cloud effects in longwave radiative transfer, *J. Atmos. Sci.*, *53*, 953–963.

Higham, N. J. (2005), The scaling and squaring method for the matrix exponential revisited, *SIAM J. Matrix Anal. Appl.*, *26*, 1179–1193.

Hogan, R. J., and A. J. Illingworth (2000), Deriving cloud overlap statistics from radar, *Q. J. R. Meteorol. Soc.*, *126*, 2903–2909.

Hogan, R. J., and J. K. P. Shonk (2013), Incorporating the effects of 3D radiative transfer in the presence of clouds into two-stream multilayer radiation schemes, *J. Atmos. Sci.*, *70*, 708–724.

Hill, P. G., C. J. Morcrette, and I. A. Boutle (2015), A regime-dependent parametrization of subgrid-scale cloud water content variability, *Q. J. R. Meteorol. Soc.*, *141*, 1975–1986.

Jensen, M. P., A. M. Vogelmann, W. D. Collins, G. J. Zhang, and E. P. Luke (2008), Investigation of regional and seasonal variations in marine boundary layer cloud properties from MODIS observations, *J. Clim.*, *21*, 4955–4973.

Kato, S., T. P. Ackerman, J. H. Mather, and E. E. Clothiaux (1999), The *k*-distribution method and correlated-*k* approximation for a shortwave radiative transfer model, *J. Quant. Spectrosc. Radiat. Transfer*, *62*, 109–121.

Klinger, C., and B. Mayer (2014), Three-dimensional Monte Carlo calculation of atmospheric thermal heating rates, *J. Quant. Spectrosc. Radiat. Transfer*, *144*, 123–136.

Lacis, A. A., and J. E. Hansen (1974), A parameterization for the absorption of solar radiation in the Earth's atmosphere, *J. Atmos. Sci.*, *31*, 118–133.

Mayer, B. (2009), Radiative transfer in the cloudy atmosphere, *Eur. Phys. J. Conf.*, *1*, 75–99.

Mayer, B., and A. Kylling (2005), Technical note: The libRadtran software package for radiative transfer calculations—Description and examples of use, *Atmos. Chem. Phys.*, *5*, 1855–1877.

Meador, W. E., and W. R. Weaver (1980), Two-stream approximations to radiative transefer in planetary atmospheres: A unified description of existing methods and a new improvement, *J. Atmos. Sci.*, *37*, 630–643.

Mlawer, E. J., S. J. Taubman, P. D. Brown, M. J. Iacono, and S. A. Clough (1997), Radiative transfer for inhomogeneous atmospheres: RRTM, a validated correlated-*k* model for the longwave, *J. Geophys. Res.*, *102*, 16,663–16,682.

Morcrette, J.-J., H. W. Barker, J. N. S. Cole, M. J. Iacono, and R. Pincus (2008), Impact of a new radiation package, McRad, in the ECMWF Integrated Forecasting System, *Mon. Weather Rev.*, *136*, 4773–4798.

Neggers, R. A. J., H. J. J. Jonker, and A. P. Siebesma (2003), Size statistics of cumulus cloud populations in large-eddy simulations, *J. Atmos. Sci.*, *60*, 1060–1074.

Pincus, R., H. W. Barker, and J.-J. Morcrette (2003), A fast, flexible, approximate technique for computing radiative transfer in inhomogeneous cloud fields, *J. Geophys. Res.*, *103*(D13), 4376, doi:10.1029/2002JD003322.

Pincus, R., C. Hannay, and K. F. Evans (2005), The accuracy of determining three-dimensional radiative transfer effects in cumulus clouds using ground-based profiling instruments, *J. Atmos. Sci.*, *62*, 2284–2293.

Schäfer, S. A. K., R. J. Hogan, C. Klinger, J. C. Chiu, and B. Mayer (2016), Representing 3D cloud-radiation effects in two-stream schemes: 1. Longwave considerations and effective cloud edge length, *J. Geophys. Res. Atmos.*, *121*, doi:10.1002/2016JD024876.

Shonk, J. K. P., and R. J. Hogan (2008), Tripleclouds: An efficient method for representing horizontal cloud inhomogeneity in 1D radiation schemes by using three regions at each height, *J. Clim.*, *21*, 2352–2370.

Shonk, J. K. P., R. J. Hogan, J. M. Edwards, and G. G. Mace (2010), Effect of improving representation of horizontal and vertical cloud structure on the Earth's radiation budget—1. Review and parameterisation, *Q. J. R. Meteorol. Soc.*, *136*, 1191–1204.

Stein, T. H. M., R. J. Hogan, P. A. Clark, C. E. Halliwell, K. E. Hanley, H. W. Lean, J. C. Nicol, and R. S. Plant (2015), The DYMECS project: A statistical approach for the evaluation of convective storms in high-resolution NWP models, *Bull. Am. Meteorol. Soc.*, *96*, 939–951.

Stephens, G. L., P. M. Gabriel, and P. T. Partain (2001), Parameterization of atmospheric radiative transfer—1. Validity of simple models, *J. Atmos. Sci.*, *58*, 3391–3409.

Tompkins, A. M., and F. Di Giuseppe (2007), Generalizing cloud overlap treatment to include solar zenith angle effects on cloud geometry, *J. Atmos. Sci.*, *64*, 2116–2125.

Waterman, P. C. (1981), Matrix-exponential description of radiative transfer, *J. Opt. Soc. Am.*, *71*, 410–422.
Várnai, T., and R. Davies (1999), Effects of cloud heterogeneities on shortwave radiation: Comparison of cloud-top variability and internal heterogeneity, *J. Atmos. Sci.*, *56*, 4206–4224.
Zdunkowski, W. G., R. M. Welch, and G. Korb (1980), An investigation of the structure of typical two-stream methods for the calculation of solar fluxes and heating rates in clouds, *Beitr. Phys. Atmos.*, *53*, 147–166.